

A Method for Three-Dimensional Time-Resolved Optical Tomography

Simon R. Arridge,¹ Jeremy C. Hebden,² Martin Schweiger,¹ Florian E.W. Schmidt,² Martin E. Fry,² Elizabeth M.C. Hillman,² Hamid Dehghani,² David T. Delpy²

¹ Department of Computer Science, University College London, Gower Street, London, WC1E 6BT

² Department of Medical Physics, University College London, Capper Street, London, WC1E 6JA

ABSTRACT: We present an overview of time-resolved optical tomography together with the hardware and software methods that we have developed for a clinical instrument that implements this modality. The hardware is based on a multichannel photon-counting technique that records the histograms of photons time-of-flight through highly scattering and attenuating media. The software is based on a finite element model that is iteratively updated in order to minimize the difference between measured and modeled data. We have presented a first experimental reconstruction of a three-dimensional (3D) distribution of variable absorption and scattering coefficient, together with an ideal simulation of the same case. © 2000 John Wiley & Sons, Inc. *Int J Imaging Syst Technol*, 11, 2–11, 2000

I. INTRODUCTION

Optical tomography has come to mean the methodology of using light in a narrow wavelength band in the near-infrared (~700–1,000 nm), to transilluminate tissue, and to use the resulting measurements of intensity on the tissue boundary to reconstruct a map of the internal optical properties. Recent developments and summaries of the state-of-the-art can be found in several review articles (Hebden et al., 1997; Arridge and Hebden, 1997; Arridge, 1999; *Philos Trans R Soc [Biol]*, 1997). We present an overview of our approach using time-resolved data acquisition methods and an iterative, finite element model-based algorithm for the reconstruction.

A. Clinical Motivation. The significant difference between the characteristic absorption of the oxygenated and deoxygenated forms of hemoglobin at optical wavelengths provides an effective means of studying the function and dynamics of certain tissues noninvasively (*Proc SPIE*, 1997). Much research has been devoted to improvements in localization of near-infrared spectroscopy (NIRS) signals and to the measurement of absolute values of the absorption coefficient, μ_a , and the (reduced) transport scattering coefficient, μ'_s , (Kienle et al., 1996; Kohl et al., 1996). Imaging represents a natural extension of these efforts, and the breast and brain have become the principal clinical targets. Research groups in Europe (Kaschke et al., 1994; Colak et al., 1997; Rinneberg et al., 1998), the United States (Fantini et al., 1999; van Houten et al., 1996; Grable et al., 1997;

Ntziachristos et al., 1998), and Japan (Oda et al., 1997) have developed optical imaging systems that are being evaluated clinically. Optical imaging of the brain offers the potential to observe the distribution of blood and to monitor the spatial and temporal variation in tissue oxygenation. Images may also reveal variation in myelination exhibited as changes in scatter. Researchers are investigating two distinct approaches to brain imaging. Two-dimensional (2D) surface mapping of the brain, although potentially very useful, is a relatively straightforward task. Multiple sources and detectors placed over the human head can monitor changes in the optical properties of the cortex and appropriate maps over the surface can be acquired (Fantini et al., 1999). Optical tomography, however, which involves reconstruction of either a 3D volume or a transverse slice, is a significantly more difficult problem (Arridge and Hebden, 1997; Colak et al., 1997; Grable et al., 1997; Pogue et al., 1995). At University College London (UCL), we have constructed an imaging system for performing optical tomography on newborn infants (Schmidt et al., 2000). This system, described in Section VII, has already been used to reconstruct 2D cross-sectional images of tissue-equivalent phantoms (Hebden et al., 1999). We present the first 3D results from this system.

B. Principles of Data Acquisition. Near-infrared imaging of the internal tissues within the infant brain must overcome the overwhelming effects of scatter that occurs when light passes through the head. Unfortunately, scatter causes absolute measurements of transmitted intensity across several centimeters of tissue to be much more strongly influenced by photon interactions at the surface than by the specific optical properties of localized regions deeper within the tissue. This has led researchers toward the development of instruments that perform measurements in the time or frequency domain (Hebden et al., 1997). The former measure the temporal distribution of photons transmitted between points on the surface in response to illumination by an impulse of light, whereas the latter determine the modulation amplitude and phase delay in response to an intensity-modulated signal. Although frequency domain systems are generally less expensive and easier to develop, current technology gives time domain a significant advantage in terms of effective temporal resolution.

Correspondence to: Simon R. Arridge

C. Imaging Principles. The general principle on which optical tomography is based is that a finite set of measurements of transmitted light between pairs of points on the surface of an object is sufficient to reconstruct an arbitrary 3D distribution of internal scatterers and absorbers. Unfortunately, the predominance of scatter prevents the use of the Radon transform and backprojection methods for all but a limited set of circumstances (Arridge and Hebden, 1997). A more productive approach to imaging is to determine the parameters that describe an appropriate model of photon transport within the investigated medium by comparing its predictions with the measured data. The model is then adjusted iteratively until acceptable correspondence is achieved. Convergence toward the correct solution is assisted by the use of appropriate regularization methods. This technique requires three distinct components: a forward model that can generate a set of reliable measurements from a given internal 2D or 3D distribution of scattering and absorbing parameters; the definition of an objective function to be minimized, based on the error between model predictions and experimental data; and a scheme for adjusting the parameters of the forward model to achieve the minimization.

D. 3D Imaging. Although some semianalytic approaches to 3D optical tomography have been suggested, these are generally limited to cases where the assumption of linearity is reasonable, i.e., where the object being imaged is a small perturbation within an otherwise well-characterized background, and require the use of difference data (i.e., the acquisition of two sets of data, with and without the perturbing object present; Cai et al., 1997). The more mathematically correct iterative techniques have so far been generally limited to 2D problems because of the computational effort involved in the reconstruction. These 2D image reconstruction implementations are frequently evaluated with data simulated by a 2D light transport model to avoid a mismatch between the data and the inverse model (Schweiger et al., 1993; Paulsen and Jiang, 1995). A simple approach to 3D imaging is to employ a tomographic setup that collects boundary data for one single plane at a time and then use a 2D reconstruction, with appropriate correction methods applied, to produce a cross-sectional image in this plane. A 3D reconstruction is then presented as a series of 2D cross-sections. Results reported of reconstructions using this approach applied to measured data have depended on the use of either difference data or on an estimated correction factor (Jiang et al., 1995, 1996; Hampel and Freyer, 1998; Schmidt et al., submitted). In a previous paper, we reported a method for full 3D image reconstruction and showed that, in the absence of reference measurements or correction factors, 2D reconstructions from 3D data would suffer from severe artifact (Schweiger and Arridge, 1998). Furthermore, in addition to artifact due to model mismatch, these methods would not account for the presence of out-of-plane structure.

II. LIGHT TRANSPORT MODELS

A general model of light transport in scattering media, but one that ignores polarization and coherence effects, is the Boltzmann equation. This equation has been extensively studied in the field of neutron transport (Davison, 1957; Weinberg and Wigner, 1958; Case and Zweifel, 1967; Duderstadt and Martin, 1997; Ackroyd, 1997) and in radiation transfer (Chandrasekhar, 1950; Ishimaru, 1978) where it is known as the radiative transfer equation (RTE). In its single-group formulation, the Boltzmann equation is written

$$\left(\frac{1}{c} \frac{\partial}{\partial t} + \hat{\mathbf{s}} \cdot \nabla + \mu_{\text{tr}}(\mathbf{r}) \right) \phi(\mathbf{r}, \hat{\mathbf{s}}, t) = \mu_s(\mathbf{r}) \int_{S^{n-1}} \Theta(\hat{\mathbf{s}}, \hat{\mathbf{s}}') \phi(\mathbf{r}, \hat{\mathbf{s}}', t) d\hat{\mathbf{s}}' + q(\mathbf{r}, \hat{\mathbf{s}}, t). \quad (1)$$

Here $\mu_{\text{tr}}(\mathbf{r}) = \mu_s(\mathbf{r}) + \mu_a(\mathbf{r})$ (units of inverse length) is the transport cross-section at position \mathbf{r} , with $\mu_s(\mathbf{r})$ the scattering cross-section and $\mu_a(\mathbf{r})$ the absorption cross-section. $\phi(\mathbf{r}, \hat{\mathbf{s}}, t)$ (units of inverse length cubed) is the number of photons per unit volume at position \mathbf{r} with velocity in angular direction $\hat{\mathbf{s}}$, with $q(\mathbf{r}, \hat{\mathbf{s}}, t)$ the number of source photons. $\Theta(\hat{\mathbf{s}}, \hat{\mathbf{s}}')$ is the normalized phase function representing the probability of scattering from direction $\hat{\mathbf{s}}'$ to direction $\hat{\mathbf{s}}$, which is usually taken to be only a function of the relative angle between these directions, i.e., $\Theta(\hat{\mathbf{s}}, \hat{\mathbf{s}}') = \Theta(\hat{\mathbf{s}} \cdot \hat{\mathbf{s}}')$.

Working with the full Boltzmann equation is computationally difficult, so we use the well-understood diffusion approximation (DA). Extensive results show that the DA is adequate in typical applications in biomedical optics. The derivation of the DA from the Boltzmann equation is described in many sources (Davison, 1957; Weinberg and Wigner, 1958; Case and Zweifel, 1967; Duderstadt and Martin, 1979; Chandrasekhar, 1950; Ishimaru, 1978); it represents the simplest nontrivial approximation that results from considering the second-order form of the spherical harmonic expansion of the Boltzmann equation. We make the following definitions

$$\text{photon density: } \Phi(\mathbf{r}, t) = \int_{S^{n-1}} \phi(\mathbf{r}, \hat{\mathbf{s}}, t) d\hat{\mathbf{s}}, \quad (2)$$

$$\text{isotropic source: } q_0(\mathbf{r}, t) = \int_{S^{n-1}} q(\mathbf{r}, \hat{\mathbf{s}}, t) d\hat{\mathbf{s}}, \quad (3)$$

$$\text{average cosine: } \Theta_1 = \int_{-1}^1 \mu \Theta(\mu) d\mu, \quad (4)$$

$$\text{reduced scattering coefficient: } \mu'_s(\mathbf{r}) = (1 - \Theta_1) \mu_s(\mathbf{r}), \quad (5)$$

$$\text{diffusion coefficient: } \kappa(\mathbf{r}) = \frac{1}{3(\mu_a(\mathbf{r}) + \mu'_s(\mathbf{r}))}, \quad (6)$$

whence the DA is given by:

$$-\nabla \cdot \kappa(\mathbf{r}) \nabla \Phi(\mathbf{r}, t) + \mu_a(\mathbf{r}) \Phi(\mathbf{r}, t) + \frac{1}{c} \frac{\partial \Phi(\mathbf{r}, t)}{\partial t} = q_0(\mathbf{r}, t). \quad (7)$$

The appropriate boundary condition is of Robin type:

$$\Phi(\mathbf{m}, t) + 2A\kappa(\mathbf{m}) \frac{\partial \Phi(\mathbf{m}, t)}{\partial \nu} = 0, \quad (8)$$

where ν is the normal to the boundary at position \mathbf{m} . The value of A is 1 for a matched refractive index medium, but otherwise depends on the refractive index mismatch at the boundary and is discussed by

several authors (Schweiger et al., 1995; Aronson, 1995; Contini et al., 1997).

III. MEASURABLES

From the field $\Phi(t)$, we can define the measurable boundary flux from Eq. (8) as

$$\Gamma(\mathbf{m}, t) = -\kappa(\mathbf{m}) \frac{\partial \Phi(\mathbf{m}, t)}{\partial \nu} = \zeta \Phi(\mathbf{m}, t), \quad (9)$$

where $\zeta = 1/(2A)$. For the system described in Section VII, where the source is a close approximation to a δ -function at time t_q , at position \mathbf{r}_q , the measured flux is effectively the Green's function of the system

$$\Gamma(\mathbf{m}, t) \simeq g_{\kappa, \mu}(\mathbf{m}, \mathbf{r}_q, t - t_q). \quad (10)$$

However, this quantity is not directly measurable by our system, due to the many unquantifiable losses of photons. Instead, we build up a histogram of the photon flight times. In effect, we normalize the quantity in Eq. (9) by the total number of photons received at a given detector, illuminated by a given source. We may express this as

$$\bar{\Gamma}(\mathbf{m}, t) \simeq \frac{g_{\kappa, \mu}(\mathbf{m}, \mathbf{r}_q, t - t_q)}{G_{\kappa, \mu}(\mathbf{m}, \mathbf{r}_q)}, \quad (11)$$

where $G_{\kappa, \mu}(\mathbf{m}, \mathbf{r}_q)$ is the Green's function of the steady-state problem.

Remark 1. We may also regard the measured histogram as the conditional probability density of a photon that reaches \mathbf{m} doing so at time t :

$$\bar{\Gamma}(\mathbf{m}, t) \equiv P(t | \mathbf{m}). \quad (12)$$

Such an interpretation may be useful in considering maximum likelihood or maximum a posteriori formulations of the problem, although we will not consider this analysis any further here.

An interesting feature of optical tomography is that, despite the time-domain problem yielding large quantities of data such that the inverse problem is nominally overdetermined, a large amount of this information is redundant. Instead of working with the full parabolic problem, we have developed methods for working with transformations of the data that yield in some sense "optimal" information. Principal among these are integral transforms of the histogram, including Fourier, Laplace, and Mellin transforms. In this paper, we consider only the Mellin transform case, which is equivalent to taking the moments (mean, variance, skew) of the probability distribution defined in Eq. (12). The measurement types we consider therefore are given by:

$$c_n = \mathcal{M}_{c_n}[\Gamma] := \frac{1}{\mathcal{E}[\Gamma]} \int_{-\infty}^{\infty} (t - \langle t \rangle)^n \Gamma(t) dt, \quad (13)$$

where

$$\mathcal{E}[\Gamma] := \int_{-\infty}^{\infty} \Gamma(t) dt \quad (14)$$

is defined as the integrated intensity over all measured times.

IV. OVERVIEW OF THE METHOD

An attractive idea is to attempt analytical inversion formulae based on the diffusion equation. These are straightforward to derive for simple cases such as infinite homogeneous space or other simple geometries (Arridge et al., 1992; Arridge, 1995; Schotland et al., 1993; Schotland, 1997). However, for the general application to complex geometries and heterogeneous tissues, computational techniques must be used. Our approach is to use a finite element method (FEM) for the forward problem, which has proved flexible and efficient (Arridge et al., 1993a; Arridge and Schweiger, 1995a; Schweiger et al., 1995; Schweiger and Arridge, 1997a). A summary of the features of this model is given in Section V; in particular, we emphasize that we do not use the FEM to compute $\bar{\Gamma}(\mathbf{m}, t)$ explicitly, but develop a scheme to compute the moments of this quantity directly in a much more efficient manner. In the inverse problem, Section VI, the moments of the experimentally obtained histograms are computed and the error between the experimental and computed moments defines a functional to be minimized. The solution is discretized into a basis (which is independent to the FEM basis) and the coefficients of this basis define the search space over which the functional is minimized. In Section VII, details of the hardware for image acquisition are described; in Section VIII, the details of an experimental test on a solid phantom are described. Results for this case, both simulated and experimental, are in given in Section IX. Finally, some conclusions are presented in Section X.

V. FINITE ELEMENT METHOD

The FEM implementation of Eq. (7) is obtained by specifying that the domain Ω is divided into P elements, joined at D vertex nodes. The solution Φ is approximated by the piecewise polynomial function $\Phi^h(\mathbf{r}) = \sum_i^D \Phi_i u_i(\mathbf{r}) \in \mathcal{U}^h$, where \mathcal{U}^h is a finite dimensional subspace spanned by basis functions $\{u_i(\mathbf{r}); i = 1 \dots D\}$ chosen to have limited support. Under these assumptions, the diffusion Eq. (7) is expressed (Arridge et al., 1993a; Schweiger et al., 1995)

$$\mathbf{F}\Phi(t) + \mathbf{B} \frac{\partial \Phi(t)}{\partial t} = \mathbf{q}(t), \quad (15)$$

where

$$\mathbf{F} = \mathbf{K}(\kappa) + \mathbf{C}(\mu) + \zeta \mathbf{A}. \quad (16)$$

The system matrices \mathbf{K} , \mathbf{C} , \mathbf{A} , and \mathbf{B} , have entries given by:

$$K_{ij} = \int_{\Omega} \kappa(\mathbf{r}) \nabla u_i(\mathbf{r}) \cdot \nabla u_j(\mathbf{r}) d^n \mathbf{r}, \quad C_{ij} = \int_{\Omega} \mu_a(\mathbf{r}) u_i(\mathbf{r}) u_j(\mathbf{r}) d^n \mathbf{r},$$

$$B_{ij} = \int_{\Omega} u_i(\mathbf{r}) u_j(\mathbf{r}) d^n \mathbf{r}, \quad A_{ij} = \int_{\partial \Omega} u_i(\mathbf{m}) u_j(\mathbf{m}) d^{n-1} \mathbf{m},$$

and the source vector \mathbf{q} has terms

$$q_i(t) = \int_{\Omega} u_i(\mathbf{r}) q_0(\mathbf{r}, t) d^n \mathbf{r}. \quad (17)$$

The solution of this system becomes one of sparse matrix inversion for the spatial variables, for which standard methods are readily available. In the results used in this paper, we used a conjugate gradient method with incomplete Cholesky preconditioning for the matrix inversion step in the forward model. In order to develop the time-varying form, $\Phi(t)$, finite differencing methods can be used, but they are computationally expensive (Arridge et al., 1993a). Instead, efficient computational methods have been developed in the FEM framework for the measurement datatypes of Section III (Arridge, 1998; Arridge and Schweiger, 1995b; Schweiger and Arridge, 1997b). Specifically, the Mellin transform of $\Phi(t)$ makes use of the relations

$$\check{\Phi}^{(n)} := \int_{-\infty}^{\infty} t^n \Phi(t) dt, \quad q_0^{(n)} := \int_{-\infty}^{\infty} t^n q_0(t) dt, \quad (18)$$

to develop the iterative scheme

$$\begin{aligned} \check{\Phi}^{(0)} &= \mathbf{G}[\mathbf{q}_0], \\ \check{\Phi}^{(n)} &= \mathbf{G}[n\mathbf{B}\check{\Phi}^{(n-1)} + \mathbf{q}_0^{(n)}], \end{aligned} \quad (19)$$

where $\mathbf{G} = (\mathbf{K}(\kappa) + \mathbf{C}(\mu) + \zeta\mathbf{A})^{-1}$ is the formal inverse of the combined system matrix in Eq. (15). The n^{th} moment around $t = 0$ is given by

$$\langle t^n \rangle = \frac{\check{\Phi}^{(n)}}{\check{\Phi}^{(0)}}, \quad (20)$$

with the moments around the mean given by standard linear combinations

$$c_n = \sum_{k=0}^n \binom{n}{k} \langle t^{n-k} \rangle \langle t \rangle^k. \quad (21)$$

The key advantage of this scheme is that the cost of solving for the n^{th} temporal moment is just n times that of solving for the steady-state intensity (Arridge and Schweiger, 1995b).

VI. IMAGE RECONSTRUCTION

We consider the reconstruction as the optimization of a functional,

$$I^{\mathcal{M}} = \frac{1}{2} \sum_{j=1}^S \sum_{i=1}^{M_j} \left(\frac{y_{j,i}^{\mathcal{M}} - F_{j,i}^{\mathcal{M}}(\kappa, \mu_a)}{\sigma_{j,i}^{\mathcal{M}}} \right)^2 + \Upsilon(\kappa, \mu_a), \quad (22)$$

where $y_{j,i}^{\mathcal{M}}$ is the data of type \mathcal{M} for the i^{th} measurement ($i = 1 \dots M_j$) from the j^{th} source ($j = 1 \dots S$) with standard deviation $\sigma_{j,i}^{\mathcal{M}}$, $F_{j,i}^{\mathcal{M}}$ is the modeled data of this type for this source-detector pair, and Υ is a functional representing prior knowledge. A variety of methods for finding a minimum of this function have been developed. In

this paper, we use a nonlinear Polak-Ribière method combined with a quadratic interpolation rule for the (inexact) line search (Arridge and Schweiger, 1998). At the heart of this method is an efficient computation of the gradient of the objective function in Eq. (22), utilizing adjoint sources.

Let $\mu_a(\mathbf{r})$ and $\kappa(\mathbf{r})$ be expressed in a basis

$$\kappa(\mathbf{r}) = \sum_{k=1}^{N_{\kappa}} \kappa_k v_k^{(\kappa)}(\mathbf{r}) \quad \mu_a(\mathbf{r}) = \sum_{k=1}^{N_{\mu}} \mu_k v_k^{(\mu)}(\mathbf{r}). \quad (23)$$

Then the system matrices \mathbf{K} , \mathbf{C} can be decomposed as:

$$\mathbf{K}(\kappa) = \sum_k^{N_{\kappa}} \kappa_k \mathbf{V}_k(\kappa) \quad \mathbf{C}(\mu) = \sum_k^{N_{\mu}} \mu_k \mathbf{V}_k(\mu), \quad (24)$$

where $\mathbf{V}_k(\kappa)$, $\mathbf{V}_k(\mu)$ have entries given by

$$\mathbf{V}_{k,ij}(\kappa) = \int_{\Omega} v_k^{(\kappa)}(\mathbf{r}) \nabla u_i(\mathbf{r}) \cdot \nabla u_j(\mathbf{r}) d^n \mathbf{r}, \quad (25)$$

$$\mathbf{V}_{k,ij}(\mu) = \int_{\Omega} v_k^{(\mu)}(\mathbf{r}) u_i(\mathbf{r}) u_j(\mathbf{r}) d^n \mathbf{r}. \quad (26)$$

Because the measurables we are considering are normalized, we need to use the quotient rule for Fréchet differentiation. The gradient \mathbf{z} , of the objective function for the mean time measurable is then a vector of length $N_{\kappa} + N_{\mu}$ whose component for basis coefficient k is given by

$$\begin{aligned} z_k^{(i)}(x) &:= \frac{\partial I^{(i)}}{\partial x_k} = - \sum_{j=1}^S [\langle \Psi_j'(A), \mathbf{V}_k(x) \Phi_j \rangle + \langle \Psi_j(A), \\ &\quad \mathbf{V}_k(x) \Phi_j \rangle - \langle \Psi_j(B), \mathbf{V}_k(x) \Phi_j \rangle], \end{aligned} \quad (27)$$

where $\Psi_j(A)$, $\Psi_j'(A)$, $\Psi_j(B)$ are the solutions to the adjoint problems

$$(\mathbf{K} + \mathbf{C} + \zeta\mathbf{A}) \Psi_j(A) = \sum_{i=1}^{M_j} \frac{(y_{j,i}^{(i)} - F_{j,i}^{(i)}) F_{j,i}^{(i)}}{\sigma_{j,i}^{(i)2} F_{j,i}^{(i)}} \mathbf{q}_i^+, \quad (28)$$

$$(\mathbf{K} + \mathbf{C} + \zeta\mathbf{A}) \Psi_j'(A) = \mathbf{B} \Psi_j(A), \quad (29)$$

$$(\mathbf{K} + \mathbf{C} + \zeta\mathbf{A}) \Psi_j(B) = \sum_{i=1}^{M_j} \frac{(y_{j,i}^{(i)} - F_{j,i}^{(i)})}{\sigma_{j,i}^{(i)2} F_{j,i}^{(i)}} \mathbf{q}_i^+, \quad (30)$$

$\Phi_j' = \check{\Phi}_j^{(1)}$ and \mathbf{q}_i^+ is an adjoint source representing the transpose of the measurement operator.

For the results presented in this paper, we use a trilinearly interpolated voxel grid as the basis for image reconstruction. The matrices $\mathbf{V}_k(x)$, which are constant throughout the iterative image reconstruction process, are computed during mesh generation and held in a sparse representation. The computational cost of computing the gradient is thus the cost of solving the forward and adjoint

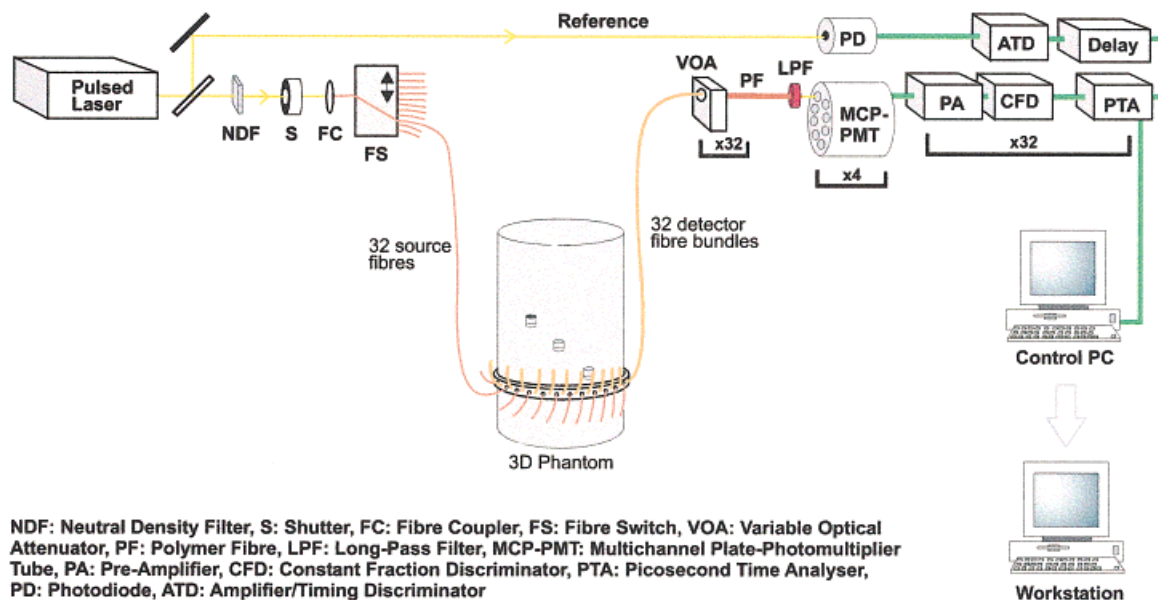


Figure 1. Diagram of the imaging instrument.

problems S times followed by the formation of $N_{\kappa} + N_{\mu}$ quadratic inner products given by Eq. (27).

VII. THE IMAGING SYSTEM

The UCL 32-channel time-resolved imaging system is illustrated in Figure 1. Picosecond pulses at a wavelength between 750 nm and 850 nm are provided by a Ti:sapphire laser pumped by a diode-pumped cw laser. The beam of pulses, attenuated to an appropriate level, passes through an electronic shutter and beam splitter, and is then coupled into a 32-way fiber switch. The 32 output fibers are held in contact with the object, and the switch enables the source to be effectively moved in discrete steps sequentially over the surface. Incident photons undergo multiple scattering as they propagate through the object. Those exiting the surface are collected simultaneously by 32 fiber bundles, approximately 2.5 mm in diameter. These bundles relay the light to 32 fully simplex ultrafast time-correlated single-photon counting (TCSPC) detectors. A large variation in source-detector fiber separation produces a correspondingly large dynamic range of intensities of light detected at the surface. Thus, in order to avoid saturation of or damage to the detectors, it is necessary to attenuate the light levels of those fiber bundles that are closest to the source. This is accomplished using 32 computer-controlled variable optical attenuators (VOAs). Intensities are typically adjusted to give count rates of the order of 10^5 counts per second (cps) per detector. The VOAs can also be used as shutters for completely blocking off channels where required. Light passing through the VOAs is collected by short large-diameter single-polymer fibers and relayed to the photocathodes of four 8-anode microchannel-plate photomultiplier tube (MCP-PMT) detectors via a long pass filter, which prevents detection of visible light. Each photon detected by the MCP-PMT produces an analogue electronic pulse that is amplified and converted into a logic pulse by the constant

fraction discriminator (CFD), which provides picosecond timing accuracy. Using a reference pulse derived from a fast photodiode illuminated directly by the laser beam, the arrival times of pulses from the CFD are measured using a picosecond time analyzer (PTA) unit. The PTA builds up a histogram of photon flight times (the TPSF), which is read out by a control PC.

The imaging instrument is known as the multichannel optoelectronic near-infrared system for time-resolved image reconstruction (MONSTIR). The temporal resolution and stability of the MONSTIR are critical for obtaining an optimum quality of image raw data. The instrument response function (IRF) of the overall system is approximately 100 ps with a temporal drift of around 5 ps per hour. The detection electronics is able to process up to around 3×10^5 cps per channel, whereas the cooled MCP-PMTs produce negligible dark counts. Further information on the construction and performance of the MONSTIR is provided by Schmidt et al. (2000).

VIII. THE 3D IMAGING EXPERIMENT

An initial experimental evaluation of the 3D facility of TOAST was performed using a solid tissue-equivalent phantom in the form of a cylinder, 140 mm in length and 70 mm in diameter (Fig. 2). The block has a nominal reduced scatter coefficient $\mu'_s = 0.85 \pm 0.10 \text{ mm}^{-1}$ and an absorption coefficient $\mu_a = 0.010 \pm 0.002 \text{ mm}^{-1}$ at a wavelength of 780 nm. Inserted within the block are three small cylinders, 10 mm in length and 8 mm in diameter. Each is located 17.5 mm from the central axis, at different heights from the base: (A) 50 mm, (B) 75 mm, and (C) 100 mm. The three cylinders were constructed with relative optical coefficients of (A) $10 \mu'_s$ and μ_a , (B) $5 \mu'_s$ and $5 \mu_a$, and (C) μ'_s and $10 \mu_a$. A black plastic ring was constructed to fit around the circumference of the phantom and to hold the 32 detector fiber bundles and 32 source fibers in contact with the surface. The ring was placed at five different heights above

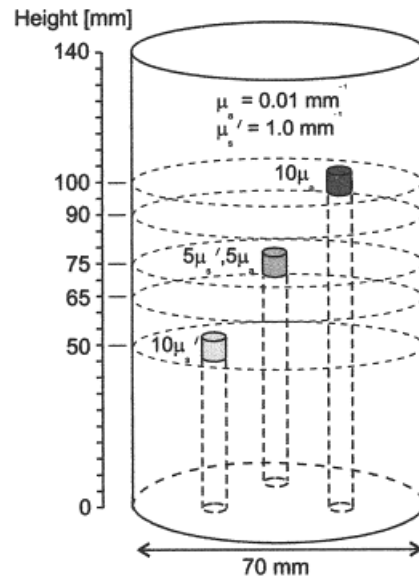
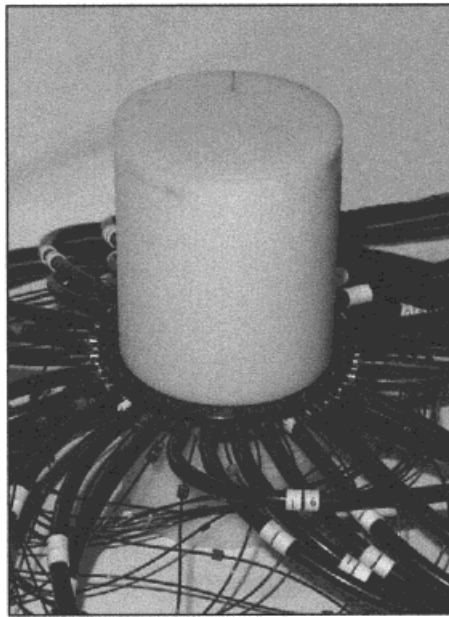


Figure 2. Photograph of the solid phantom and diagram of the location of objects.

the base of the block: 50, 65, 75, 90, and 100 mm (Fig. 2). A preprogrammed data acquisition protocol was performed automatically under computer control for each of the five scans. The VOAs ensured that the photon count rates did not exceed around 3×10^5 photons per second per channel, and deactivated the 10 detectors closest to each source because they required attenuation beyond their dynamic range. Each of the 32 sources was illuminated consecutively, and TPSFs were recorded simultaneously at 22 positions immediately opposite each activated source for 15 s, producing a total of 3,520 measurements for the five ring positions.

For this first ever test of our 3D reconstruction method using experimental data, it was decided to reduce the complexity of the problem by performing a simultaneous reconstruction for absorption and scatter using only one datatype, the mean time of each TPSF. Mean time requires compensation for the effect of differences in lengths of source fibers, detector bundles, and electronic cables, as well as the finite temporal response of the system. This was achieved via calibration measurements.

Every attempt has been made to develop a calibration protocol suitable for the future application of the instrument to the clinical

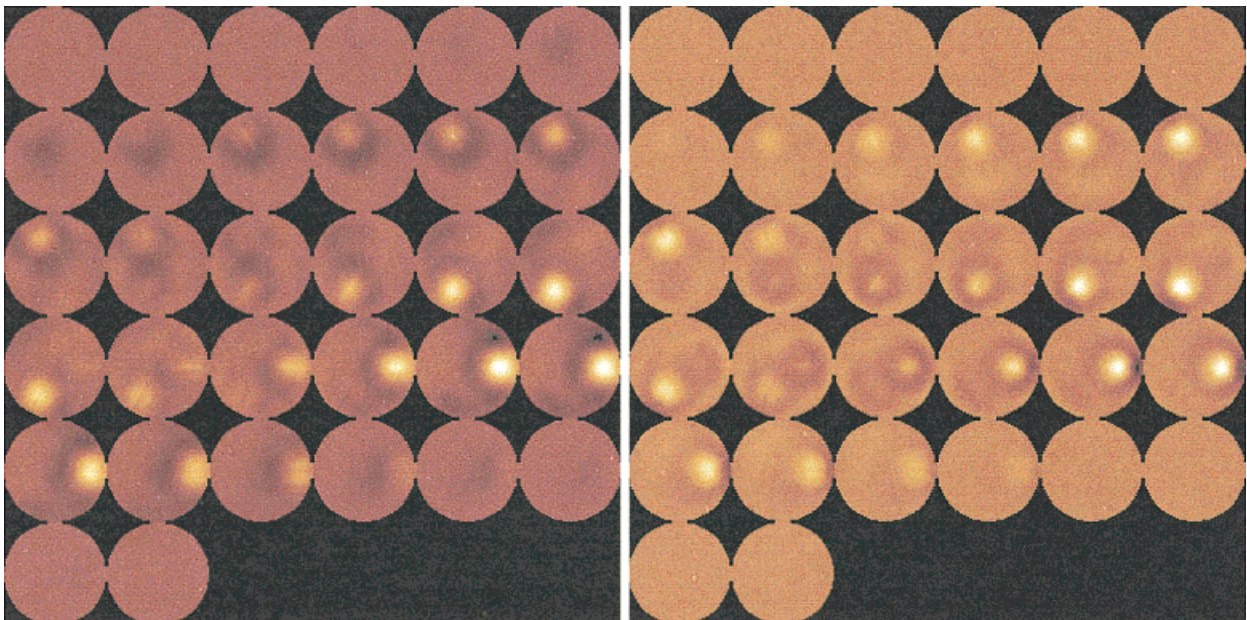


Figure 3. 3D reconstruction of absorption and scatter from simulated mean time data.

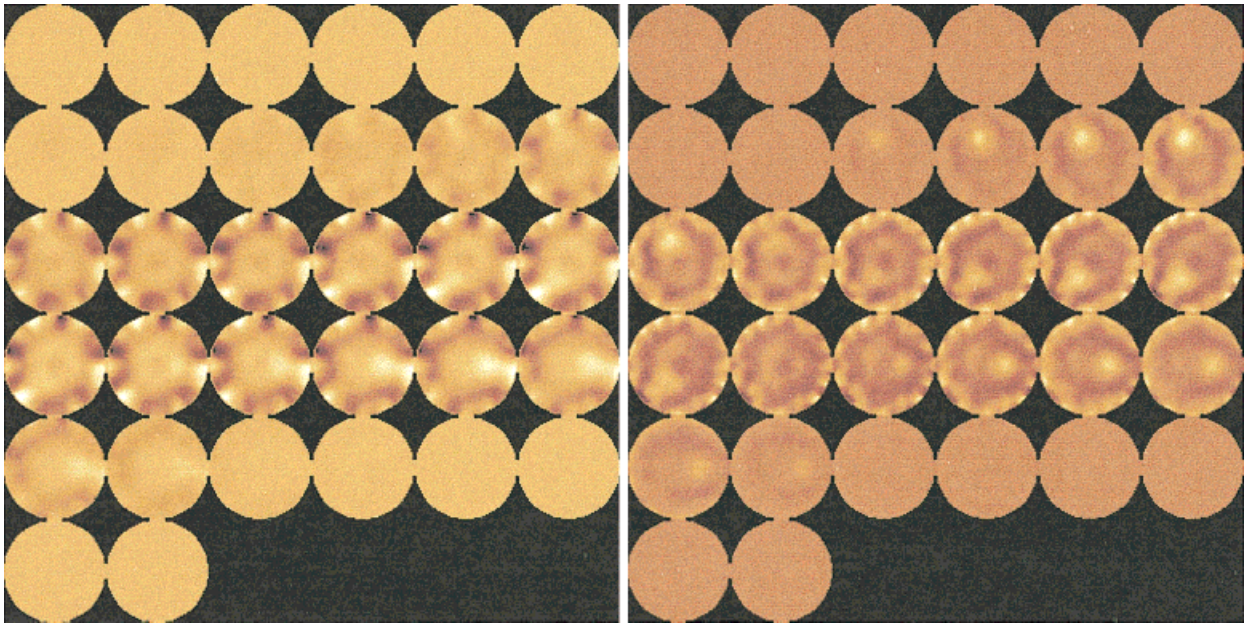


Figure 4. 3D reconstruction of absorption and scatter from experimental mean time data.

environment. We use specially constructed calibration tools to collect temporal information about all 32 sources and detectors. Described in detail in Schmidt et al., 2000, these tools are designed to provide calibration measurements prior to image acquisition on an object of arbitrary head-like geometry and properties. We can then derive the appropriate correction factors for all 1,024 possible source-detector combinations and apply them to the mean times calculated from the image data TPSFs. The images shown in Figure 4 used only these calibration measurements.

In addition to the above methods, a second calibration measurement was acquired during the imaging experiment. The central plane of a homogeneous phantom with similar geometry and background optical properties to the structured phantom was imaged. The data acquired on this phantom represent a measurement of all 1,024 unique impulse responses of the source-detector combinations. In addition, these data will depend to an extent on the properties of the homogeneous phantom. The use of these data to perform a calibration has been found to better eliminate features caused by systematic experimental errors. This may be because the noise characteristics of the TPSFs measured here will be similar to those measured on the structured phantom, and the relation between individual source-detector pairs is being measured directly (rather than indirectly in the case of the calibration mentioned above). This means that any systematic error that affects mean time, and is common to the imaging and calibration measurements, will be more effectively eliminated. Although acquisition of such a calibration measurement requires more time, and the construction and use of such a calibration tool in the clinical environment may prove impractical, processing is greatly simplified. The images in Figure 5 show significantly less artefact than those in Figure 4.

Note that this phantom is not used as a method of determining absolute values of optical parameters, or to calibrate for nonlinearity. In the images shown, the mismatch between the absolute properties of the structured and homogeneous phantom are unaccounted

for, as is the fact that the calibration measurement was only taken in the central plane of the homogeneous phantom. Despite this, the measurement was effective in calibrating each plane of data collected at different heights on the structured phantom. Although these factors are no doubt affecting quantitation, they do suggest that the accuracy of the match between a calibration phantom and a clinical subject may not be so critical. In addition, the influence of the properties of the homogeneous phantom on the calibration process could be eliminated with further processing, allowing extraction of the 1,024 correction factors alone (Hillman et al., submitted).

IX. RESULTS

A. Comparison of Data with FEM Forward Model. To obtain an estimate for the initial parameter set of the reconstruction, we compared calibrated measured data to the 3D forward-modeled datatypes of homogeneous cylinders of different optical properties.

The background values found were $\mu_a = 0.011 \text{ mm}^{-1}$ and $\mu'_s = 0.85 \text{ mm}^{-1}$, keeping refractive index and reflection term A at their nominal values. Other datatypes (variance about the mean and Laplace) were used to corroborate these estimated optical properties such that the forward-modeled datatypes agreed well with all three datatypes derived from the experimental TPSF (after calibration). The global values obtained by this fitting procedure were input as the initial distribution for the results in the following sections.

B. Simulated Experiment. In order to estimate the ideal performance of the inverse procedure, a 3D reconstruction from simulated data was performed using the same measurement geometry as the actual experiment. The optical background properties used by the forward data generator were set to $\mu_a = 0.011 \text{ mm}^{-1}$, $\mu'_s = 0.85 \text{ mm}^{-1}$, $n = 1.56$, and $A = 3.778$, to match the parameters believed to occur in the experimental data, as determined by the fitting procedure of the previous section. Perturbations were added to the model with positions and relative contrasts the same as for the experimental phantom.

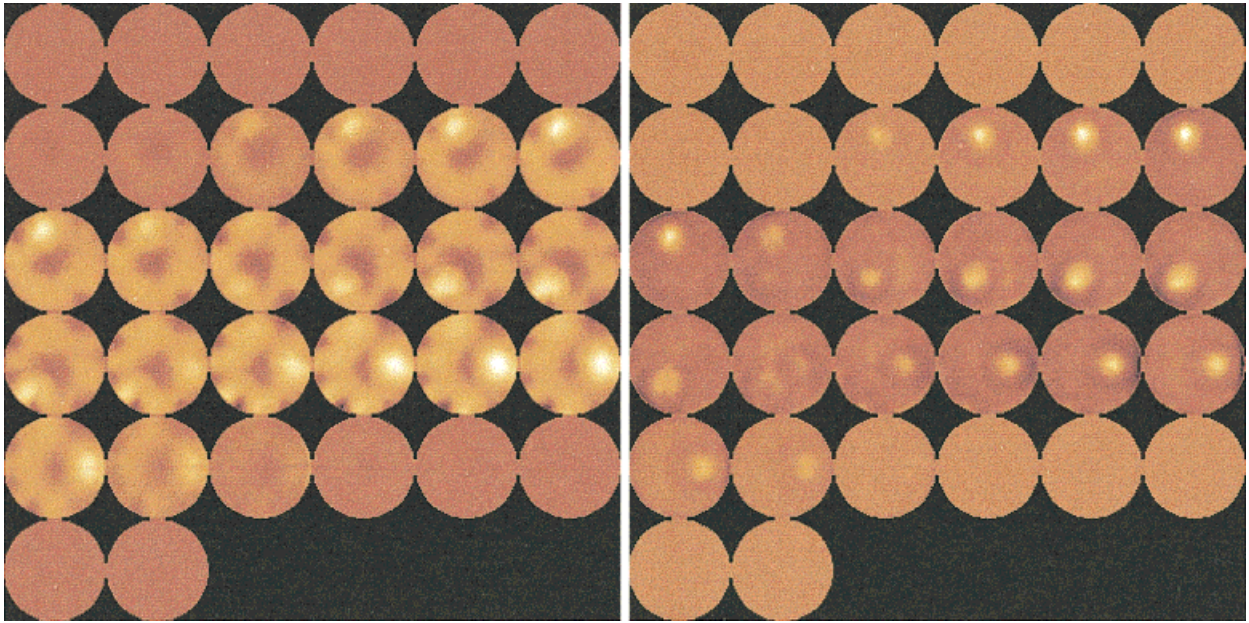


Figure 5. 3D reconstruction of absorption and scatter from experimental mean time data, using a homogeneous calibration phantom.

At each step of the reconstruction, the update is filtered using a $3 \times 3 \times 3$ median filter to suppress noise while preserving high-contrast features. The result acquired after 16 iterations is shown in Figure 3. This shows 32 transverse slices across the reconstructed volume from the bottom of the phantom (top left image) to the top (bottom right image). Bright regions corresponding to all three simulated cylinders are evident, centered at the expected lateral and vertical positions.

It is interesting to note that the absorbing cylinder still appears in the reconstructed image of the scattering properties and the scattering cylinder in the reconstructed image of the absorbing properties. This is due to the cross-talk that inevitably occurs when reconstruction for a single parameter is performed, because absorption as well as scatter has a perturbing effect on mean time measurement. According to a conjecture in Arridge (1999), two “orthogonal” measurement types are required to separate absorption and scatter. In the case of mean time, the presence of an embedded region with increased absorption will result in a decrease in mean time measurement for every source-detector pair. However, the effect of an increase in scatter is less straightforward. A positive perturbation in scatter can produce a temporal delay, which increases mean time, but also results in increased local absorption, which has the opposite effect. Which effect dominates will depend somewhat on the relative positions of the source, detector, and perturbing region. This complex behavior, which has been observed previously with 2D reconstructions, may have given rise to the negative ring artefact around the expected position of the scattering cylinder in Figure 3.

C. Measured Data. The reconstruction algorithm was employed to generate 3D absorbing and scattering maps from the experimental data, using the same mesh and inversion procedure employed for the simulated data. The result obtained after 16 iterations is shown as a series of 32 slices in Figure 4. The scattering map clearly reveals the presence of three scattering cylinders in the correct 3D positions,

with the “true” scattering cylinder (A) having the strongest amplitude, and the “false” cylinder (i.e., the absorber C) having the weakest. The absorbing map has the opposite results, with cylinder C having the strongest amplitude and cylinder A the weakest.

It is obvious that the images are contaminated by considerable artefact, with the absorption image worse than the scatter image. One difficulty is the precise determination of source-detector positions. The artefacts are also similar to those seen in early simulation studies (Arridge et al., 1993b). In those studies, we suggested the use of regularization schemes that showed considerable improvement in the images. In particular, we introduced the idea of a spatially varying regularization scheme that was designed to reduce boundary artefacts. These schemes have not yet been implemented in 3D and so are not employed here.

Finally, we show in Figure 5 the case where we first subtract from the data, measurements from a homogeneous phantom of similar size to that shown in Figure 2, but with different optical properties. In this case, the extra calibration arising from using the actual signal levels and coupling characteristics of a typical measurement considerably reduces the artefacts, although cross-talk is still prevalent.

X. CONCLUSIONS

We have presented a summary of the hardware and software methods that we have developed for time-resolved optical tomography. The hardware is based on a multichannel photon-counting technique that records the histograms of photons time-of-flight through highly scattering and attenuating media. The software is based on an FEM that is iteratively updated in order to minimize the difference between measured and modeled data. We have presented the first experimental reconstruction of a 3D distribution of variable absorption and scattering coefficients, together with an ideal simulation of the same case.

Obviously more work is required to validate our 3D reconstruction facility, using experiments with different acquisition geometries and reconstructions with multiple datatypes. Due to computational restraints, we have not been able to run an extensive number of trials to investigate the consequence of using different datatypes, mesh sizes, initial parameters, and regularization methods. However, the results of this first attempt are encouraging. We are confident that current efforts to optimize the experimental method and the reconstruction algorithm will result in substantial improvements to the experimental results.

Debate as to the relative merits of different instruments and reconstruction software is difficult to judge without comparative experimental cases. Therefore, we have made our data, phantoms, and software available via the website of the UCL biomedical optics research group www.medphys.ucl.ac.uk/research/borg.

ACKNOWLEDGMENTS

Support for this research has been generously provided by the Wellcome Trust.

REFERENCES

- R.T. Ackroyd, Finite element methods for particle transport: Applications to reactor and radiation physics, Research Studies Press, Taunton, United Kingdom, 1997.
- R. Aronson, Boundary conditions for diffusion of light, *J Opt Soc Am [A]* 12 (1995), 2532–2539.
- S.R. Arridge, Photon measurement density functions. Part 1: Analytical forms, *Appl Opt* 34 (1995), 7395–7409.
- S.R. Arridge, Optical tomography in medical imaging, *Inverse Problems* 15 (1999), R41–R93.
- S.R. Arridge, M. Cope, and D.T. Delpy, Theoretical basis for the determination of optical pathlengths in tissue: Temporal and frequency analysis, *Phys Med Biol* 37 (1992), 1531–1560.
- S.R. Arridge and J.C. Hebden, Optical imaging in medicine: II. Modeling and reconstruction, *Phys Med Biol* 42 (1997), 841–853.
- S.R. Arridge and M. Schweiger, Photon measurement density functions. Part 2: Finite element calculations, *Appl Opt* 34 (1995a), 8026–8037.
- S.R. Arridge and M. Schweiger, Direct calculation of the moments of the distribution of photon time of flight in tissue with a finite-element method, *Appl Opt* 34 (1995b), 2683–2687.
- S.R. Arridge and M. Schweiger, A gradient-based optimisation scheme for optical tomography, *Opt Express* 2 (1998), 213–226.
- S.R. Arridge, M. Schweiger, M. Hiraoka, and D.T. Delpy, A finite element approach for modeling photon transport in tissue, *Med Phys* 20 (1993a), 299–309.
- S.R. Arridge, M. Schweiger, M. Hiraoka, and D.T. Delpy, Performance of an iterative reconstruction algorithm for near infrared absorption and scatter imaging, *Proc SPIE* 1888 (1993b), 360–371.
- W. Cai, B.B. Das, F. Liu, F.A. Zeng, M. Lax, and R.R. Alfano, “Three dimensional image reconstruction in highly scattering turbid media,” *Optical tomography and spectroscopy of tissue: Theory, instrumentation, model and human studies*, B. Chance, R. Alfano (Editors), SPIE 2979, Bellingham, WA, USA, 1977, pp. 241–244.
- M.C. Case and P.F. Zweifel, *Linear transport theory*, Addison-Wesley, New York, 1967.
- S. Chandrasekhar, *Radiative transfer*, Oxford University Press, London, 1950.
- S.B. Colak, D.G. Papaioannou, G.W. 't Hooft, M.B. van der Mark, H. Schomberg, J.C.J. Paasschens, J.B.M. Melissen, and N.A.A.J. van Asten, Tomographic image reconstruction from optical projections in light-diffusing media, *Appl Opt* 36 (1997), 180–213.
- D. Contini, F. Martelli, and G. Zaccanti, Photon migration through a turbid slab described by a model based on diffusion approximation. 1 theory, *Appl Opt* 36 (1997), 4587–4599.
- B. Davison, *Neutron transport theory*, Oxford University Press, London, 1957.
- J.J. Duderstadt and W.R. Martin, *Transport theory*, Wiley, New York, 1979.
- S. Fantini, M.A. Franceschini, E. Gratton, D. Hueber, W. Rosenfeld, D. Maulik, P.G. Stubblefield, and M.R. Stankovic, Non-invasive optical mapping of the piglet in real time, *Opt Express* 4 (1999), 308–314.
- R.J. Grable, D.P. Rohler, and K.L.A. Sastry, “Optical tomography in breast imaging,” *Optical tomography and spectroscopy of tissue: Theory, instrumentation, model and human studies*, B. Chance, R. Alfano (Editors), SPIE 2979, Bellingham, WA, USA, 1997, pp. 197–210.
- U. Hampel and R. Freyer, Fast image reconstruction for optical tomography in media with radially symmetric boundaries, *Med Phys* 25 (1998), 92–101.
- J.C. Hebden, S.R. Arridge, and D.T. Delpy, Optical imaging in medicine: I. Experimental techniques, *Phys Med Biol* 42 (1997), 825–840.
- J.C. Hebden, F.E.W. Schmidt, M.E. Fry, M. Schweiger, E.M.C. Hillman, D.T. Delpy, and S.R. Arridge, Simultaneous reconstruction of absorption and scattering images by multichannel measurement of purely temporal data, *Opt Lett* 24 (1999), 534–536.
- E.M.C. Hillman, J.C. Hebden, F.E.W. Schmidt, S.R. Arridge, M. Schweiger, and D.T. Delpy, Calibration techniques and datatype extraction for time-resolved optical tomography, *Rev Sci Instr* (submitted).
- A. Ishimaru, *Wave propagation and scattering in random media* (Vol. 1), Academic Press, New York, 1978.
- H. Jiang, K.D. Paulsen, and U.L. Osterberg, Optical image reconstruction using dc data: Simulations and experiments, *Phys Med Biol* 41 (1996), 1483–1498.
- H. Jiang, K.D. Paulsen, U.L. Osterberg, B.W. Pogue, and M.S. Patterson, Optical image reconstruction using frequency-domain data: Simulations and experiments, *J Opt Soc Am [A]* 13 (1995), 253–266.
- M. Kaschke, H. Jess, G. Gaida, J. Kaltenbach, and W. Wrobel, Transillumination imaging of tissue by phase modulation techniques, *Adv Opt Imaging Photon Migration* 21 (1994), 88–92.
- A. Kienle, L. Lilge, M.S. Patterson, R. Hibst, R. Steiner, and B.C. Wilson, Spatially resolved absolute diffusive reflectance measurements for noninvasive determination of the optical scattering and absorption coefficients of biological tissue, *Appl Opt* 35 (1996), 2304–2314.
- M. Kohl, R. Watson, and M. Cope, Determination of absorption-coefficients in highly scattering media from changes in attenuation and phase, *Opt Lett* 21 (1996), 1519–1521.
- V. Ntzichristos, X. Ma, and B. Chance, Time-correlated single photon counting imager for simultaneous magnetic resonance and near-infrared mammography, *Rev Sci Instruments* 69 (1998), 4221–4233.
- M. Oda, Y. Yamashita, H. Kan, H. Miyajima, A. Sawaki, T. Nakano, S. Suzuki, A. Suzuki, K. Shimizu, S. Muramatsu, N. Sugiura, K. Ohta, and Y. Tsuchiya, “Advanced devices for nir time resolved spectroscopy and optical computed tomography,” *Optical tomography and spectroscopy of tissue: Theory, instrumentation, model and human studies*, B. Chance, R. Alfano (Editors), SPIE 2979, Bellingham, WA, USA, 1997, pp. 765–773.
- K.D. Paulsen and H. Jiang, Spatially-varying optical property reconstruction using a finite element diffusion equation approximation, *Med Phys* 22 (1995), 691–701.
- Philos Trans R Soc [Biol], Near-infrared spectroscopy and imaging of living systems, B. Chance, C.E. Cooper, D.T. Delpy, E.O.R. Reynolds (Editors), 352 (1997).

- B.W. Pogue, M.S. Patterson, H. Jiang, and K.D. Paulsen, Initial assessment of a simple system for frequency domain diffuse optical tomography, *Phys Med Biol* 40 (1995), 1709–1729.
- Proc SPIE, Optical tomography and spectroscopy of tissue: Theory, instrumentation, model and human studies II, B. Chance, R. Alfano (Editors), 2979 (1997).
- H. Rinneberg, D. Grosenick, H. Wabnitz, H. Danlewski, K. Moesta, and P. Schlag, Time-domain optical mammography: Results on phantoms, healthy volunteers, and patients, M. Patterson, J. Fujimoto (Editors), *Adv Opt Imaging Photon Migration* 21 (1998), 278–280.
- F.E.W. Schmidt, M.E. Fry, J.C. Hebden, E.M.C. Hillman, and D.T. Delpy, A 32-channel time-resolved instrument for medical optical tomography, *Rev Sci Instruments* 71(1) (2000), 256–265.
- F.E.W. Schmidt, J.C. Hebden, E.M.C. Hillman, M.E. Fry, M. Schweiger, D.T. Delpy, and S.R. Arridge, Multiple slice imaging of a tissue-equivalent phantom using time-resolved optical tomography, *Appl Opt* (submitted).
- J.C. Schotland, Continuous-wave diffusion imaging, *J Opt Soc Am [A]* 14 (1997), 275–279.
- J.C. Schotland, J.C. Haselgrove, and J.S. Leigh, Photon hitting density, *Appl Opt* 32 (1993), 448–453.
- M. Schweiger and S.R. Arridge, The finite element model for the propagation of light in scattering media: Frequency domain case, *Med Phys* 24 (1997a), 895–902.
- M. Schweiger and S.R. Arridge, Direct calculation of the Laplace transform of the distribution of photon time of flight in tissue with a finite-element method, *Appl Opt* 36 (1997b), 9042–9049.
- M. Schweiger and S.R. Arridge, Comparison of 2D and 3D reconstruction algorithms in optical tomography, *Appl Opt* 37 (1998), 7419–7428.
- M. Schweiger, S.R. Arridge, and D.T. Delpy, Application of the finite-element method for the forward and inverse models in optical tomography, *J Math Imaging Vision* 3 (1993), 263–283.
- M. Schweiger, S.R. Arridge, M. Hiraoka, and D.T. Delpy, The finite element model for the propagation of light in scattering media: Boundary and source conditions, *Med Phys* 22 (1995), 1779–1792.
- J.P. van Houten, D.A. Benaron, S. Splilman, and D.K. Stevenson, Imaging brain injury using time-resolved near infrared light scanning, *Pediatr Res* 39 (1996), 470–476.
- A.M. Weinberg and E.P. Wigner, *The physical theory of neutron chain reactors*, University of Chicago Press, Chicago, 1958.